Volume 13
Number 48
28 December 2025
Pages 41405–42480

Journal of Materials Chemistry A

Materials for energy and sustainability

rsc.li/materials-a

ISSN 2050-7488

ROYAL SOCIETY OF CHEMISTRY

PAPER
Mingyuan Ge, Yu-chen Karen Chen-Wiegart *et al.*
Spatial and chemical heterogeneity in aqueous Zn/MnO_2 batteries: role of Zn and Mn containing complexes

Journal of
Materials Chemistry A

ROYAL SOCIETY
OF CHEMISTRY

PAPER

View Article Online
View Journal | View Issue

Cite this: *J. Mater. Chem. A*, 2025, **13**, 41734

Spatial and chemical heterogeneity in aqueous Zn/MnO_2 batteries: role of Zn and Mn containing complexes

Varun R. Kankanallu,[a] Xiaoyin Zheng,[a] Chang-An Lo,[a] Andrew Kiss,[b] Evan Musterman,[b] Ajith Pattammattel,[b] Amy C. Marschilok,[acde] Esther S. Takeuchi,[acde] Kenneth J. Takeuchi,[acde] Xiaojing Huang,[b] Mingyuan Ge *[b] and Yu-chen Karen Chen-Wiegart *[ab]

Received 11th March 2025
Accepted 11th September 2025

DOI: 10.1039/d5ta02014j

rsc.li/materials-a

Aqueous Zn/MnO_2 batteries are a promising, safe alternative for grid-scale energy storage, owing to their environmentally safe and low-cost nature. The dissolution–deposition reaction mechanism in a mild aqueous pH regime has recently gained significance due to its relevance in battery design. Comprehending both the specific locations and the way reaction progresses is crucial for efficient batteries. This study demonstrates that Zinc Hydroxy Sulfate (ZHS) formed during discharge primarily near the dissolved MnO_2 particles. Acting as a host for charge reactants in subsequent cycles, the charge product morphology was visualized using *operando* X-ray fluorescence microscopy. After ~400 hours of cycling, capacity fade was linked to the formation of a Zn–Mn core–shell phase which is attributed to an irreversible core phase in the electrode, visualized through three-dimensional chemical mapping. Overall, this research underscores the importance of understanding local morphological evolution in designing electrodes and chemistries for advanced grid-scale energy storage technologies.

1. Introduction

The development of green and eco-friendly battery technology is essential in transforming towards renewable energy sources. There is a need for developing energy storage systems for managing peak demands and integrating sustainable energy sources, namely solar radiation, wind and wave.[1,2] For large scale energy storage systems, a low cost, environmentally benign, high cycle life and high-power capability surpasses the need for high energy density.[3–7] Aqueous batteries serve as a suitable alternative to Li-ion batteries (LIBs) due to the concerns on the higher cost and scarcity of raw materials of LIBs. Among various aqueous battery systems, aqueous Zn–MnO_2 batteries stand out as a promising alternative due to the abundance and safety of their materials, attracting significant research attention in recent years.[8–12]

The current limitation in using aqueous Zn–MnO_2 battery as secondary batteries is in its poor cycle life since the charge storage reaction mechanism is not well understood. Various reaction mechanisms and their corresponding failure mechanisms have been proposed for aqueous Zn–MnO_2 battery.[13–19] Specifically, the dissolution and deposition reaction mechanism of Zn–MnO_2 batteries has gathered importance for elucidating the discharge and charge plateaus during electrochemical cycling.[20–22] Godeffroy *et al.* proposed that the dissolution/deposition of MnO_2 is the main reaction pathway and that the phase control obtained by the synthesis is lost in the subsequent cycles. This work also indicates that the short-range order and the potential amorphous phase formed by electrodeposited MnO_2 and precipitates are difficult to analyze using laboratory X-ray diffraction or spectroscopic techniques.[23] Chen *et al.* proposed that the micro-sized flakes of $Zn_4SO_4(OH)_6\cdot nH_2O$ (ZHS) behave as the reactant, which induce the deposition reaction to form layered vernadite ($Zn_xMnO(OH)_2$) nanosheets. These nanosheets reversibly transform back into ZHS, directing the subsequent reaction mechanism.[22] Surface sensitive nano-imaging and electron diffraction have helped to explain how chalcophanite phase ($ZnMn_3O_7\cdot 3H_2O$) nucleates and grows on the ZHS; in addition to the chalcophanite phase, which is deemed to be reversible, an irreversible hetaerolite phase ($ZnMn_2O_4$) was proposed to be forming on the surface of the electrode during charging; the formation of $ZnMn_2O_4$ may

---

[a] *Department of Materials Science and Chemical Engineering, Stony Brook University, Stony Brook, NY, 11794, USA. E-mail: Karen.Chen-Wiegart@stonybrook.edu*
[b] *National Synchrotron Light Source II, Brookhaven National Laboratory, Upton, NY, 11973, USA. E-mail: mingyuan@bnl.gov*
[c] *Department of Chemistry, Stony Brook University, Stony Brook, NY, 11794, USA*
[d] *Energy and Photon Sciences Directorate, Brookhaven National Laboratory, Upton, NY 11973, USA*
[e] *Institute of Sustainability, Electrification, and Energy (I:SEE), Stony Brook University, Stony Brook, NY, 11794, USA*

further inhibit the reaction leading to capacity fade and degradation.[24]

With significant progress on addressing the fundamental mechanism of dissolution/deposition in Zn–MnO_2 batteries, there remains a need to study morphological evolution of the MnO_2 electrode by probing the reversibility of ZHS formation and dissolution by differentiating the chemical species forming in the latter cycles. Additionally, it should be noted that the H_2O molecule can be easily extracted from the crystal structure of ZHS and Zn–Mn phase highlighting the need of *operando* techniques for studying the phase evolution of the electrode dissolution and deposition mechanism.[21,25] Being able to resolve these morphological and chemical changes with a multimodal, multi-scale characterization approach is key for improving our fundamental understanding and ultimately enabling better design for future batteries.[26]

In this work, a combination of *operando* and *ex situ* X-ray imaging synchrotron characterization is implemented at varying length scale from electrode to individual active particles of the β-MnO_2 active material. β-MnO_2 has a narrower 1 × 1 tunnel structure, which makes Zn^{2+} ion intercalation challenging.[18] Mapping the evolution of elemental distribution in electrodes and interphases reveals the formation of ZHS during discharge. Additionally, the phase formed near the dissolving MnO_2 particles during subsequent charging was also identified. Preferential dissolution of the smaller sized MnO_2 particles and the morphological evolution around the larger particles was visualized and quantified using quasi-*in situ* X-ray nanotomography. Finally, the failure mechanism of the electrode indicated that the growth of Zn–Mn phases inhibits further reaction progress on the electrode visualized with chemical phase sensitive 3D spectroscopic imaging. Overall, the site of the reaction, along with the prevalence and spatial distribution of ZHS, and the subsequent formation of Zn–Mn phases, all contribute to the functioning and eventual failure of the battery. This understanding of the reaction mechanism and reaction heterogeneity at latter cycles will aid the continuing development of electrode architecture for stationary energy storage systems that are key to a sustainable energy future.

2. Results and discussion

2.1 Local heterogeneity of the Mn and Zn phases by *operando* synchrotron X-ray fluorescence imaging

Operando synchrotron X-ray fluorescence imaging was conducted to study the spatial distribution of the Mn and Zn phases during the discharge and charge processes for the first four cycles of β-MnO_2 cathode material. The schematic of the *operando* XRF setup is represented in Fig. 1a. The *operando* battery was cycled in the range of 1–1.8 V potential range at a current rate of 0.1C for the first cycle followed by a rate of 0.2C for the subsequent second to fourth cycle. 2 M $ZnSO_4$ with 0.1 M $MnSO_4$ was used as the electrolyte. X-ray fluorescence (XRF) maps were taken during the discharge and charge process in the planar view of the electrode. Fig. 1b shows the *operando* Mn XRF map prior to electrochemical cycling. The bright spots in the XRF maps indicate the cluster of Mn which corresponds to the β-MnO_2 active material. Summing over all the pixels in the Mn or Zn XRF maps yields the quantitative measurement of the Mn or Zn phase within the map. In the *operando* configuration, the local electrolyte in the vicinity of particles would also contribute to the overall Zn and Mn signals in the XRF maps. *Operando* XRF scans were alternated with one position which remained the same (fixed position) and another position which was sequentially chosen between four different positions (floating positions) to mitigate beam damage (see Fig. S1). Additional information regarding the *operando* configuration and geometry is described in Experimental section 5.2.1.

To spatially resolve the Mn and Zn phases forming in the electrode, two regions of interest were selected in the pristine electrode: one containing clearly visible particles (dashed white box in Fig. 1b) and another with minimal visible features, indicative of an electrolyte rich region (dotted green box in Fig. 1b). These regions were chosen based on the initial Mn XRF signal intensity and morphological contrast observed in the pristine state. The particle-containing region exhibited a higher Mn signal, corresponding to the presence of MnO_2 particles, while the electrolyte region showed minimal Mn signal, likely due to the absence of particles or their presence outside the imaging depth. Fig. 1c and d shows the Mn and Zn XRF maps in these two regions marked with the dashed and the dotted box in Fig. 1b. Fig. 1e represents the sum of all pixels in the region with particles and with electrolyte for the Mn and Zn XRF signals measured at different time points, corresponding to different electrochemical cycling states. The sum of the Mn XRF signals in the region with particles and electrolyte shows a similar trend: at the end of the discharge step there is steeper decrease in the Mn signal in region with particles (indicated by grey line in Fig. 1e) in comparison with the electrolyte region, indicating the dissolution of the MnO_2 phase of the electrode. In addition, in the first cycle, corresponding to a 0.1C rate, the region with the particles shows a steeper decrease in comparison with region with the electrolyte which can be attributed to primarily the dissolution of the MnO_2 phase of the electrode, which then forms Mn^{2+} ions and diffuses into the electrolyte. This dissolution of MnO_2 phase is consistent with the proton-coupled electro dissolution mechanism represented by eqn (1) and previously reported in literature.[20,21,27]

$$MnO_2 + 2H_2O + 2e^- \rightarrow Mn^{2+} + 4OH^- \tag{1}$$

In the subsequent cycles, as the battery is cycled at a higher cycling rate of 0.2C, the Mn XRF signal exhibits distinct trends in different regions. In both the electrolyte and particle regions, a slight increase in the total Mn XRF signal is observed during discharge, while a decrease occurs during charge. This behavior can be attributed to the accumulation of Mn^{2+} ions in the electrolyte during the discharge, followed by a minimal decrease in the Mn signal during the charge half cycle. However, when considering the overall Mn XRF signal over time, a gradual decline is observed. This long-term decrease is consistent with the experimental geometry, where the cathode side of the coin cell was positioned upstream, with the MnO_2 active materials facing downstream. The XRF detector was

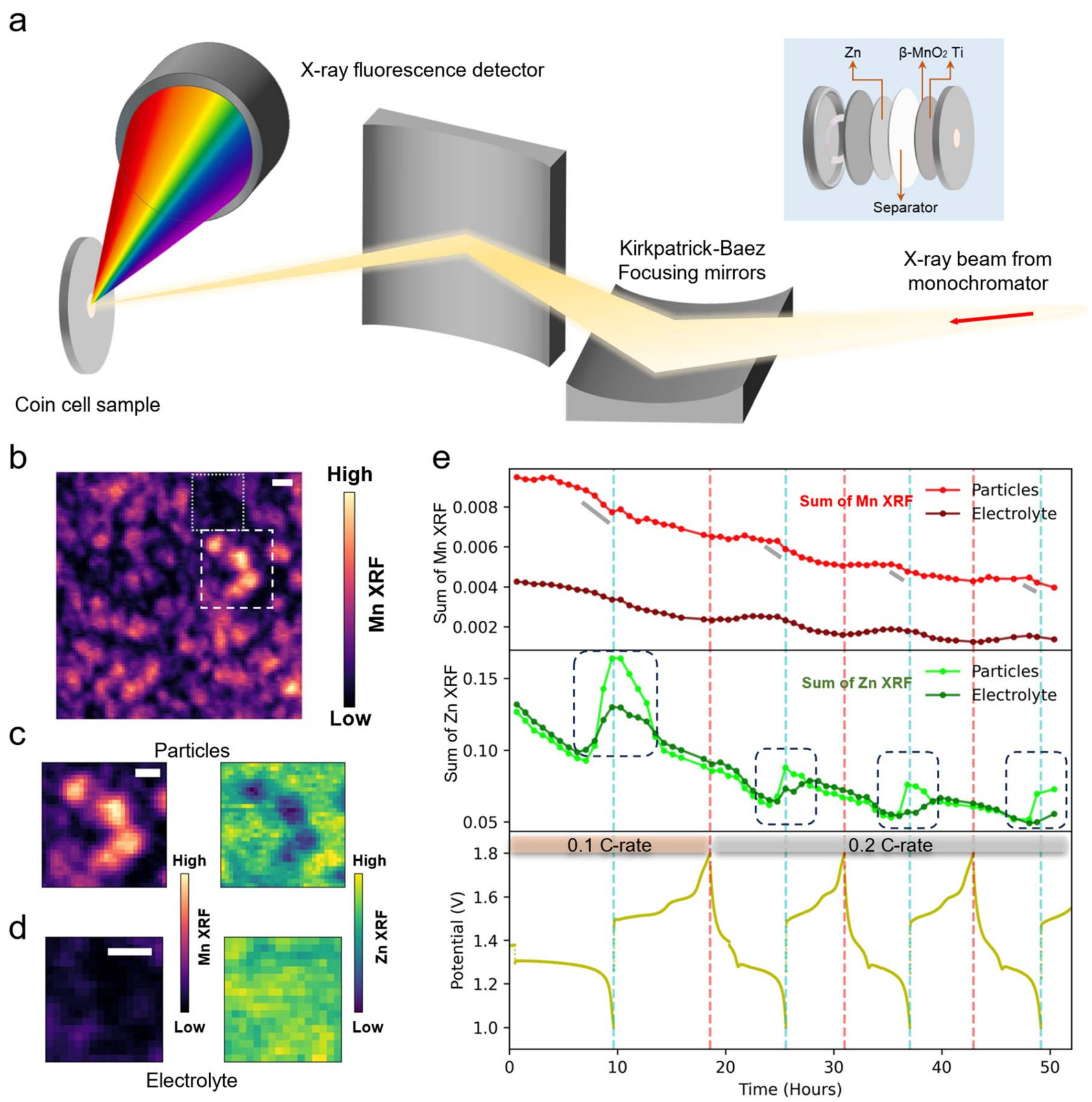

Fig. 1 *Operando* X-ray fluorescence (XRF) microscopy to study the local heterogeneity of the Mn and Zn phases. (a) A schematic of the *operando* XRF setup, with an inset showing the configuration of the coin cell positioned parallel to the X-ray beam at SRX beamline, NSLS-II. (b) Mn XRF map for the pristine state of the electrode, prior to *operando* cycling. The scale bar indicates 5 μm. Mn and Zn XRF maps containing regions with (c) particles and (d) with electrolyte as indicated by the dashed white and dotted green box respectively in (b). The scale bars indicate 3 μm. (e) Sum of XRF signals for Mn and Zn corresponding to the Mn and Zn concentration within the particles and electrolyte regions. The 1st cycle corresponds to a C-rate 0.1C whereas the 2nd–4th cycle corresponds to a C-rate of 0.2C. The XRF signals are plotted against the voltage profile collected during the electrochemical cycling.

positioned upstream of the cell. As the Mn ions moved from the MnO_2 particles into the electrolyte, they became further away from the XRF detector. As a result, the Mn XRF signals were attenuated more by the electrolyte and electrode itself. Although some Mn deposited back to the electrode, the deposition occurred mostly near the surface of the electrode, away from the XRF detector, and hence the Mn XRF signals were still attenuated more compared to the signals from the MnO_2 particles prior to dissolution, consistent with the overall decreasing trend of the Mn XRF signals. The difference in observance of the Zn signal compared to the Mn signal may also be due to the attenuation of the lower energy Mn XRF signal (5.89 keV) relative to the heavier Zn XRF signal in the electrolyte (8.64 keV). The 3D visualization of the location of these reaction products is presented in the later section of this work.

To verify the reproducibility of the sum of Mn and Zn XRF results the sum of all pixels in the field of view was analyzed at both fixed and floating positions, each covering an area of approximately 90 μm × 90 μm (see Fig. S2). A similar trend to that shown in Fig. 1e is observed.

In addition, β-MnO_2 crystalline phase was studied with X-ray micro-diffraction (μ-XRD) in the third to fourth cycle of the *operando* XRF microscopy. The μ-XRD measurement was taken at the same particle position for the third cycle charge to the fourth cycle discharge (see Fig. S3a). The (110) peak seems to be decreasing without any shift indicating the dissolution of the MnO_2 particle (see Fig. S3b). The 2D XRD pattern can be seen in Fig. S3c–e. The experimental parameters regarding particle tracking are described in Experimental section 5.2.2.

On observing the trend in the sum of the Zn XRF signals at the end of first half cycle, a significant increase in the Zn concentration is observed in the region with particles and with electrolyte at the end of the discharge process. Relatively higher change is observed in the region with particles indicating a higher concentration of Zn phase in the vicinity of the particles during discharge. Based on prior study by Kankanallu *et al.*, which implemented *in situ* synchrotron X-ray diffraction for Zn/β-MnO_2 in a mild aqueous 2 M $ZnSO_4$ + 0.1 M $MnSO_4$ electrolyte. Zinc hydroxide sulfate ($Zn_4SO_4(OH)_6 \cdot xH_2O$, ZHS) phase was identified as a major phase during discharge, further verified by Rietveld refinement.[21] Additionally, Liu *et al.* demonstrated in their *in situ* XRD study of aqueous Zn/β-MnO_2 electrodes that the ZHS phase forms during the discharge state.[28] Higher change in Zn signal in the region with particles can hence be attributed to the formation of ZHS in the vicinity of MnO_2 particles during discharge. This local formation of ZHS can be attributed to the increase in OH^- due to the dissolution of MnO_2 during the discharge half cycle as shown in eqn (1) (ref. 21 and 22) and is further represented by eqn (2).

$$4Zn^{2+} + SO_4^{2-} + 5H_2O + 6OH^- \rightarrow Zn_4SO_4(OH)_6 \cdot 5H_2O \quad (2)$$

In the subsequent second to fourth cycles, a similar increase in Zn XRF signals, corresponding to the formation of Zn-containing phases, is visible during discharge with a higher increase in the region with the particles. The increase of the Zn-containing phase at 0.2C is lower than at 0.1C, indicating a transport-limited formation of ZHS.

Furthermore, the evolution of the Mn- and Zn-XRF signal is visualized in Fig. 2. As shown in Fig. 2a, the smaller Mn-rich clusters seem to be dissolving. In the pristine electrode, the uniform Zn signal observed in Fig. 2b originates from Zn^{2+} ions in the infiltrating $ZnSO_4$ electrolyte rather than from any solid Zn-containing phase. Shell-like structures are visible during the discharge state in the Zn XRF maps, indicating a dense growth of the ZHS phase around the MnO_2 particles (see white arrows in Fig. 2b) The theoretical discharge capacity for the reduction of MnO_2 from Mn^{4+} to Mn^{2+} is 616 mAh g^{-1}. However, since only about one-fourth of this capacity ($\sim$150 mAh g^{-1}) was achieved in this experiment (see Fig. S4), the presence of dense shell of Zn-containing phase forming on the MnO_2 surface in the dissolution region may be a factor in not reaching the theoretical capacity. This dense shell of Zn phase growth around the MnO_2 particles may be causing a diffusion barrier, preventing further dissolution of the MnO_2 during the discharge half cycle of the battery. In the electrolyte regime, Zn signal shows periodic change during the discharge/charge cycle, indicating that the discharge product is primarily rich in the Zn phase and that a large range of mass transportation of Zn ions is present throughout the electrode. The ZHS phase is most prominent near the end of the discharge and during the first plateau in the charge state (see Fig. S5). This is further supported by *operando* XRD based phase quantifications which show that ZHS phase is absent at the end of charge and early discharge states of β-MnO_2 and α-MnO_2 cathode material in the initial cycles.[21,29] In the latter charge states, Zn XRF signal is visible in the same location as the ZHS formed in the discharge state (see the yellow arrows in the 2nd and 3rd cycle charge states of Fig. 2c). This indicates the colocalization of the Mn- and Zn-containing XRF signal as visible in white box in the latter cycles of Fig. 2c. The use of $MnSO_4$ as an electrolyte additive facilitates this behavior by providing an additional source of Mn^{2+}, which promotes the formation of Zn and Mn containing complexes.

The distribution and growth of Mn and Zn containing complexes in the vicinity of particles and electrolytes is further studied by quantifying the Mn and Zn XRF signals along a line profile. The line profile study for the *operando* XRF scans indicates the local evolution of Mn- and Zn-containing phases during the electrochemical process. Fig. 3a depicts the line profile across which the Mn and Zn XRF signals are counted over. The line profile (see Fig. 3a) has regions with both the electrolyte and MnO_2 particles to study heterogeneity of the electrochemical reaction. The Mn and Zn XRF line profiles are taken at the end of the discharge (Fig. 3b) and charge (Fig. 3c) electrochemical states for the first four cycles. The Mn XRF line profiles taken at the end of discharge indicate the decrease in intensity of the Mn XRF signal, as seen in the top plot of Fig. 3b. This can be attributed to the dissolution of MnO_2 particles during the discharge state.[20,21,27] The Zn XRF line profiles indicate the formation of Zn phases, namely the ZHS complex phase in the vicinity of the particles. The dotted lines in Fig. 3b indicate the highest intensity peaks of the first cycle discharge state in the Zn XRF line profile. For the second to fourth cycle in Fig. 3b, the highest intensity peak shifts towards the dissolving MnO_2 particle indicating the local growth of the ZHS phase in the close vicinity of dissolution of MnO_2 particles. For the charge state the Mn XRF line profiles become broader in the direction of the dissolved MnO_2 particles, with every subsequent scan having a lower XRF intensity. For the charge state Zn XRF line profiles, a similar shift towards the right of the dotted line is observed for second to fourth cycle charge state. Since both Zn and Mn XRF signals colocalize in this region, this is indicative of the formation of a Zn and Mn containing charged species in the close vicinity of the dissolved particles and the formed ZHS precipitate during the discharge half cycle. To further understand this preference of the growth of the charge species in the vicinity of the particles, a comparison is made for the shaded region in Fig. 3c. A higher intensity of the Zn XRF signal is prevalent for later cycles of the region near the particles in comparison to the electrolyte indicating the preferred deposition of the of Zn containing charged species or a build-up of Zn phase from the previous cycles (see Fig. 3d). The same analysis was conducted in other regions of the XRF maps (see Fig. S6) to strengthen these findings. It can therefore be hypothesized that this preferred colocalized deposition of the Zn and Mn containing phase grow on the ZHS phase, as also discussed in the literature.[21,23]

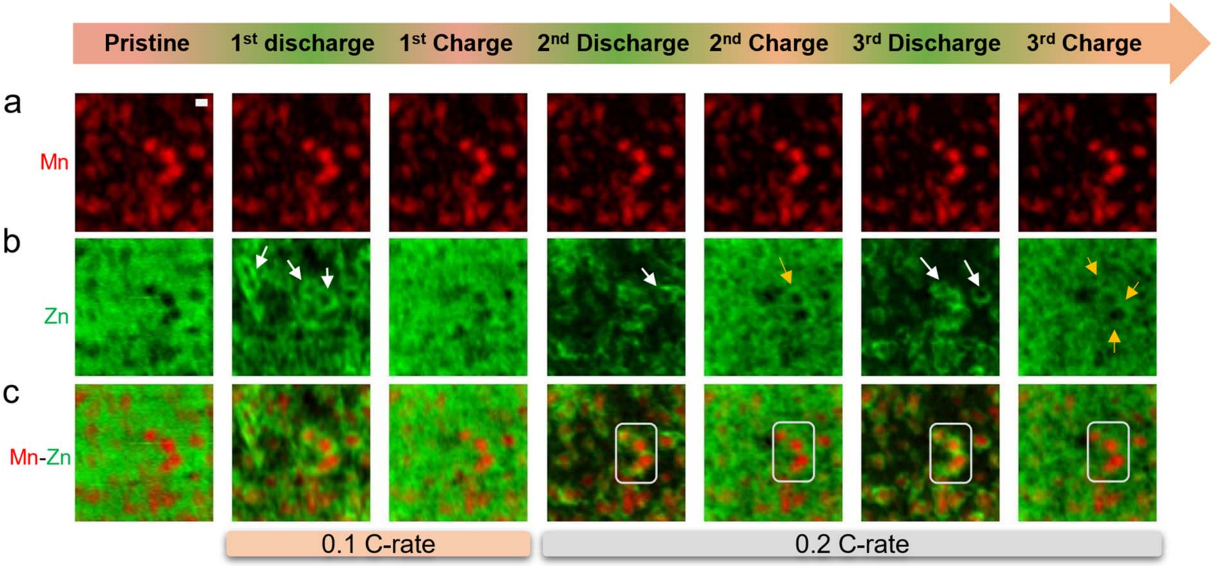

Fig. 2 Evolution of the Mn (red) and Zn (green) phases during the *operando* XRF measurement of the MnO_2 cathode material. (a and b) Respective Mn and Zn XRF maps in the pristine state, first to third discharge and charge states of the cathode. (c) Overlay of the Mn and Zn XRF maps indicating the colocalization of the Mn–Zn phases during the discharge and charge processes. The 1st cycle corresponds to a C-rate 0.1C whereas the 2nd–4th cycle corresponds to a C-rate of 0.2C. The scale bar is 5 μm. All XRF maps are on the same scale.

To investigate the evolution of the Mn- and Zn-containing phases during *operando* measurements, XRF line profiles for Mn and Zn are plotted based on the XRF maps measured during the 3rd cycle discharge (see Fig. 3e) and the 3rd cycle charge (see Fig. 3f) electrochemical states. Minimal changes were observed in the Mn XRF line profiles. In contrast, significant variations were observed in the Zn-containing phase near the 3rd cycle discharge state and the subsequent 3rd cycle charge state. As the system approached the end of the 3rd discharge state, the region with particles appeared to form a higher concentration of Zn-containing phases compared to the electrolyte region. Similarly, when the system was approaching the end of the 3rd charge state, the particle region exhibited a relatively higher Zn XRF signal in the region near the MnO_2 particles than the electrolyte region (see Fig. 3d).

To assess the chemical heterogeneity of the Mn and Zn phases forming on the electrode surface X-ray absorption near edge spectroscopy (XANES) imaging was conducted on the MnO_2 electrode after *in situ* XRF mapping. The *in situ* electrochemistry was stopped midway through the 5th cycle discharge state (see Fig. S7). Fig. S7a and b shows the X-ray attenuation across the Mn and Zn K-edge for the electrode. K-means clustering across the Mn edge identified two distinct phases (see Fig. S7c), namely the pristine MnO_2 phase and the reduced Zn–Mn phase. The reduced Zn–Mn phase as seen in the dotted box of Fig. S7d has a pre-edge feature shifted towards the left, indicating the Mn^{4+} state from the pristine state was reduced. The average Zn phase at this electrochemical state shows similarity to the standard phase[21] formed during the first cycle discharge highlighting presence and formation of a ZHS phase and the colocalized presence of the reduced Mn phase (see Fig. S7e). Information regarding the XANES imaging data processing is described in the Experimental section 5.2.4.1.

In summary, the *operando* XRF studies presented here provide spatially resolved insights and visual evidence of Zn–Mn phase co-localization during electrochemical cycling. Prior studies have utilized *in situ* Raman spectroscopy to monitor surface phase evolution of ZHS electrodes during charging, revealing the presence of layered manganese oxides, and *operando* optical microscopy to visualize dynamic heterogeneity during the cycling.[22,23] Transmission electron microscopy (TEM) has also been widely used, primarily in *ex situ* studies, to provide nanoscale structural and compositional information of the cathode materials.[24] While these techniques offer valuable insights into local structural and morphological changes, our work provides complementary insights by enabling element-specific chemical speciation at the electrode scale. In particular, this study captures the real-time distribution and evolution of Zn- and Mn-containing phases within the electrode microstructure, offering a comprehensive understanding of the spatially resolved reaction pathways. The key findings from the *operando* study are summarized below:

- A higher concentration of Zn XRF signal is seen in the regions of the particles in comparison with electrolyte indicating the strong colocalization of the ZHS phase with the dissolving MnO_2 particles during discharge.
- Correlating *operando* Mn and Zn XRF line-profile maps at the end of the charge states indicate a higher concentration of Zn near the particles indicating that the charge colocalized Zn–Mn species may be building up during the charge state.
- Correlating *operando* Mn and Zn line-profile maps of the local Zn–Mn complex formation across electrode particles demonstrates that the pristine electrode architecture may influence the local reaction environment and subsequent product evolution.

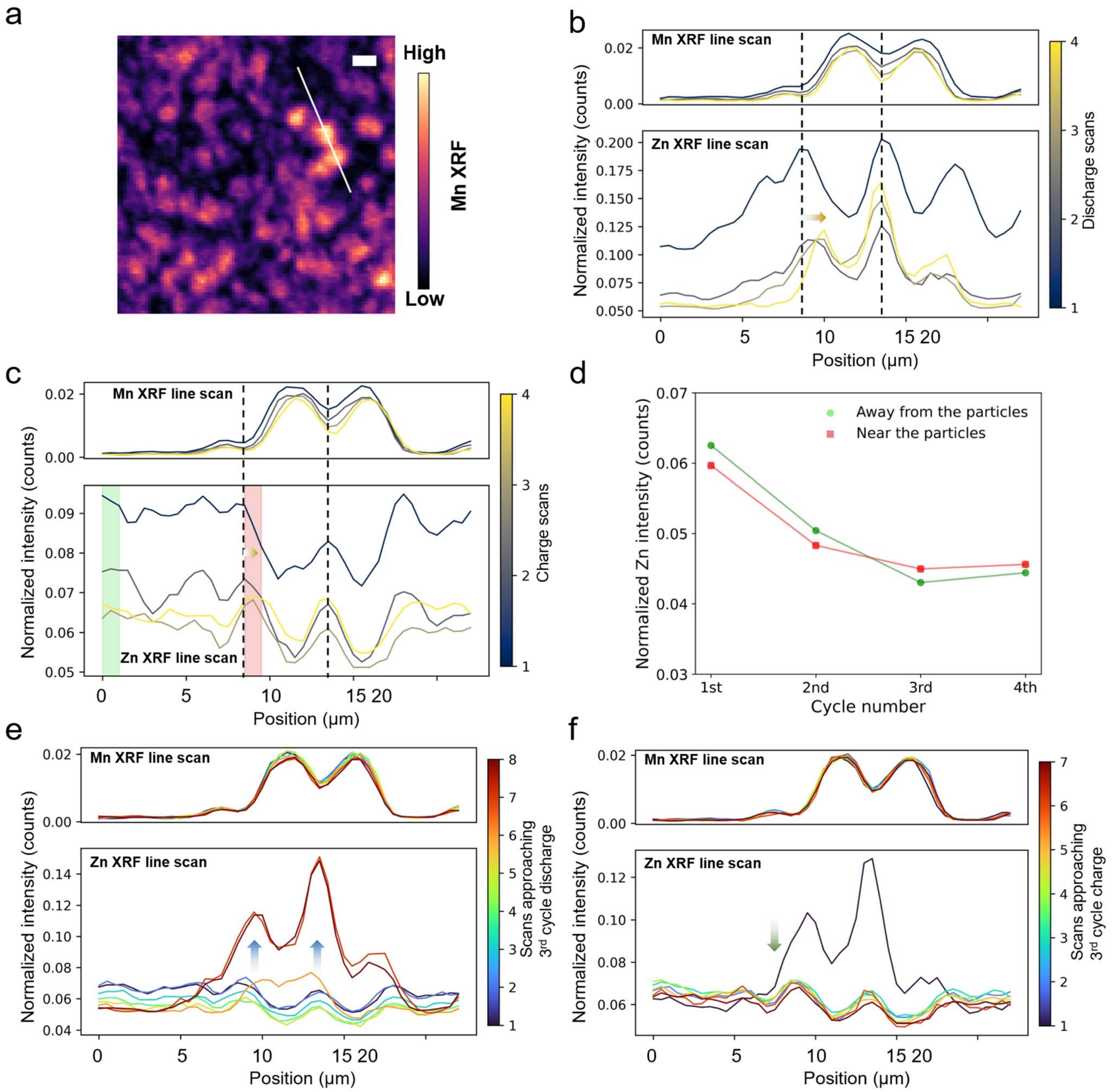

Fig. 3 Evolution of the Mn and Zn distribution characterized by XRF line profile. The analysis was done on regions with MnO_2 particles and electrolyte. (a) Mn XRF image of the pristine state MnO_2 cathode with a white line indicating the line profile along which the Mn and Zn XRF intensity is counted. The Mn and Zn XRF line profiles extracted from the XRF maps collected at the end of the (b) discharge and (c) charge electrochemical states for the first four cycles. (d) Comparison of the Zn XRF signal average in the regions near the particles and in the electrolyte. The Mn and Zn XRF line profiles extracted from the XRF collected during the (e) 3rd cycle discharge and (f) 3rd cycle charge electrochemical states. The scale bar in (a) indicates 5 μm.

2.2 Quasi-*in situ* X-ray nano-tomography to quantify morphological evolution of MnO_2 electrodes

To further visualize this morphological evolution at tens of nanometer resolution in 3D, transmission X-ray microscopy was introduced. The schematic of the quasi-*in situ* X-ray nano-tomography is presented in Fig. 4a. The setup implements a Zn/β-MnO_2 battery in a capillary geometry (see Fig. 4a). This arrangement allows for capturing projections over a nearly 180-degree range, facilitating effective 3D tomographic reconstruction. The battery was cycled through three electrochemical states: partially discharged, fully discharged, and fully charged. Tomography was measured at each of these states. The electrochemical voltage profile is presented in Fig. S8. All measurement parameters, including discussion on cell geometry, reconstruction and processing, are discussed in Experimental section 5.2.3.

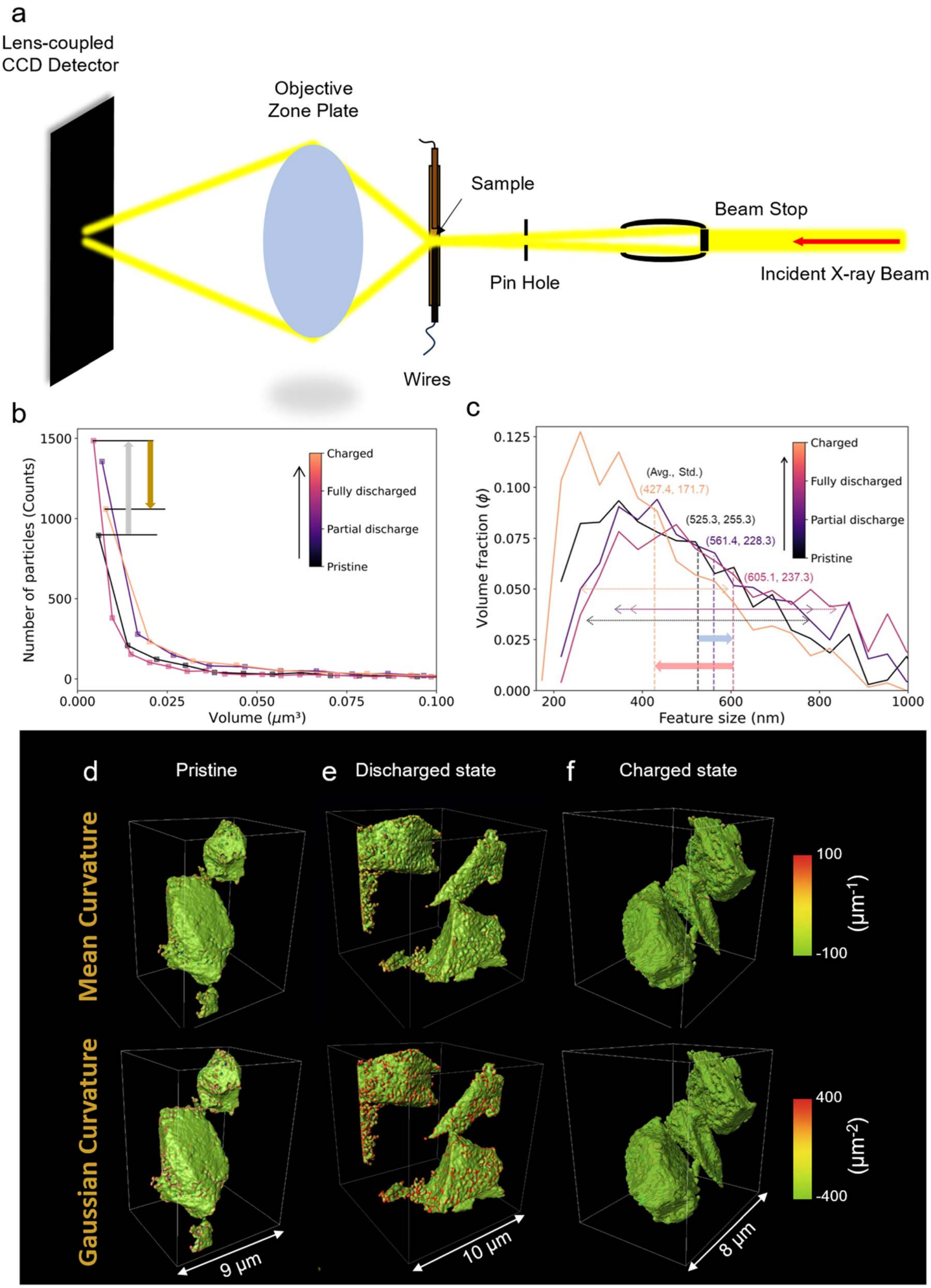

Fig. 4 Quasi-*in situ* X-ray nano-tomography to study the 3D morphological evolution of the Zn/β-MnO_2 battery. (a) Schematic of the quasi-*in situ* transmission X-ray microscopy (TXM) setup. (b) Plot showing the size distribution of MnO_2 particle volumes. (c) Particle size distribution (PSD) indicating the volume fraction of MnO_2 particles within a given feature size range. The vertical and horizontal dashed lines on the PSD plot represent the mean of the feature size (avg.) and the standard deviation of the mean feature size (std), respectively. (d–f) Mean and Gaussian curvature of the selected large β-MnO_2 particles at different electrochemical states to quantify the surface morphology of the Mn- and Zn-containing phases. The red spots in (e) show the growth of ZHS phase, corresponding to the location with high curvatures.

A plot showing the volumetric distribution of particle sizes with a β-MnO_2 electrode at various states of charge is presented in Fig. 4b. A steep initial decline in counts with increasing particle volume is observed for all states, suggesting a variation of the smaller particles with electrochemical states. For the different electrochemical states, the number of small particles increases as the state changes from pristine to the fully discharge state (grey arrow in Fig. 4b). This is attributed to the preferential dissolution of the higher surface area, smaller particles of MnO_2 during discharge. In the charged state, the number of smaller particles decreases to an extent greater than the pristine state (brown arrow in Fig. 4b) suggesting the partial reversibility of dissolved particles. The particle size distribution (PSD) plot illustrates the volumetric distribution of particle sizes for the different electrochemical states (see Fig. 4c). As the electrode evolves towards the discharge state the peak of the PSD plot shifts towards the right (light blue arrow in Fig. 4c) indicating an increase in particle size. This is also indicated by the increase in the mean of the feature size from 525.3 nm to 605.1 nm. This could be attributed to the growth of the ZHS phase over the surface of dissolving MnO_2 particles. In the charge state a reversal in the PSD towards the left of the pristine state indicates that the charged species has a smaller particle size than the pristine MnO_2 particles. This is supported by the decrease in the mean of the feature size from 605.1 nm to 427.4 nm.

The results from the previous section indicate that the discharge and charge phases primarily form near the surface of the active material. To study the morphology of the discharged and charged species in the quasi-*in situ* configuration, large particles from the tomography volume were selected and further visualized. A curvature analysis based on interfacial shape distribution (ISD)[30] was implemented to quantify the surface morphology of large particles. An ISD reflects the probability of finding a patch on interface with a given pair of maximum and minimum principal curvatures. The ISD quantitatively represents the interfacial shape of the surface of the electrode. The horizontal and vertical axes in the ISDs correspond to the minimum principal curvature (κ_1) and maximum principal curvature (κ_2), respectively. Fig. S9 shows the ISDs of the three electrochemical states for the large particles. The principal curvatures were normalized by the characteristic length (l_c), defined as the ratio of the volume to the surface area of the region of interest, to eliminate the size effect. All three ISDs are similar with the charged state having a relatively lower concentration along its axes. Furthermore, the principal curvatures can be used to represent the surface shape in an alternative way: the mean curvature, $H = (\kappa_1 + \kappa_2)/2$, and the Gaussian curvature, $K = \kappa_1 \times \kappa_2$. The mean and gaussian curvatures for the different electrochemical states can be seen in Fig. 4d–f. The magnitude for the mean and gaussian curvatures are relatively low and are negative indicated by the green shade. For the pristine state the curvatures have a higher concentration along the edges (see Fig. 4d). For the discharge state the curvatures have concentrated spots throughout the surface of the large particles. This is indicative of a pointed and rough surface morphology due to the dissolution of the MnO_2 and the formation of plate like ZHS phase (see Fig. 4e). In addition, formation of a plate-like structure is visible mostly perpendicular to the MnO_2 surface characterized by the red dots in Fig. 4e. In the charged stated these concentrated structures are not visible and a smoother surface is observed characterized by the low curvature value even along the edges (see Fig. 4f). This suggests a more uniform, potentially amorphous phase, as crystalline structures often exhibit more pronounced surface features or higher curvature due to their ordered structure. Data processing, including the curvature analysis, is described in the Experimental section 5.2.3.

2.3 2D and 3D XANES imaging analysis: probe of chemical heterogeneity of MnO_2 electrodes

The quasi-*in situ* analysis provided the morphological evolution of the Zn/β-MnO_2 battery cathode without discussing the composition of the chemical species. To study the chemical and spatial heterogeneity of the battery electrode throughout the battery operation two datasets were considered namely the mid cycled data corresponding to 160 hours of operation and after longer cycle of 400 hours of operation. A combination of 2D and 3D X-ray absorption near edge spectroscopy (XANES) imaging was conducted. 2D and 3D XANES imaging is a technique which provides us with a XANES spectra across the absorption K-edge for every pixel in 2D or a voxel of the 3D volume.[31] In this work, 8th and 32nd cycle charged electrodes (corresponding to ~160 and ~400 hours of cycling) were extracted from the battery, 2D and 3D chemical mapping was done across the Mn and Zn K-edges. The electrochemical data is depicted in Fig. S10 and S11. Due to the large number of spectra obtained from every voxel of the 3D volume, an unsupervised machine learning model was introduced.[32] K-means clustering was implemented based on an initial guess of the number clusters involved to identify the regions associated with different chemical species.[32–34] All data processing and filtering are discussed in the Experimental section 5.2.4.

For the 2D XANES analysis across the Mn K-edge, two distinct regions were identified (see Fig. 5a), corresponding to two average XANES spectra: the MnO_2 phase (shown in red) and the Zn–Mn complex phase (shown in green) (see Fig. 5c). The MnO_2 phase appears to have dissolved, as shown in Fig. 5a, while the Zn–Mn phase is dispersed throughout the electrode, with concentrations surrounding the MnO_2 particles. The standard spectra correspond to the Mn K-edge spectrum of pristine β-MnO_2 (indicated by a dotted red line) and the 8th cycle charge electrode (indicated by a dotted green line), derived from bulk X-ray absorption spectroscopy data from previous work.[21] The average spectrum aligns closely with their respective standards, as shown in the dotted box in Fig. 5c.

The Zn chemical map reveals two well-distributed phases, labeled Zn–Mn phase 1 and Zn–Mn phase 2 (as seen in Fig. 5b). These Zn–Mn phases are distributed across the electrode and resemble different proportions of FEFF-calculated spectra for $ZnMn_3O_7$ and $ZnMn_2O_4$ phases (see Fig. 5d). In the chemical map, Zn–Mn phase 1 appears to nucleate in isolated regions, while Zn–Mn phase 2 forms a denser layer over the electrode

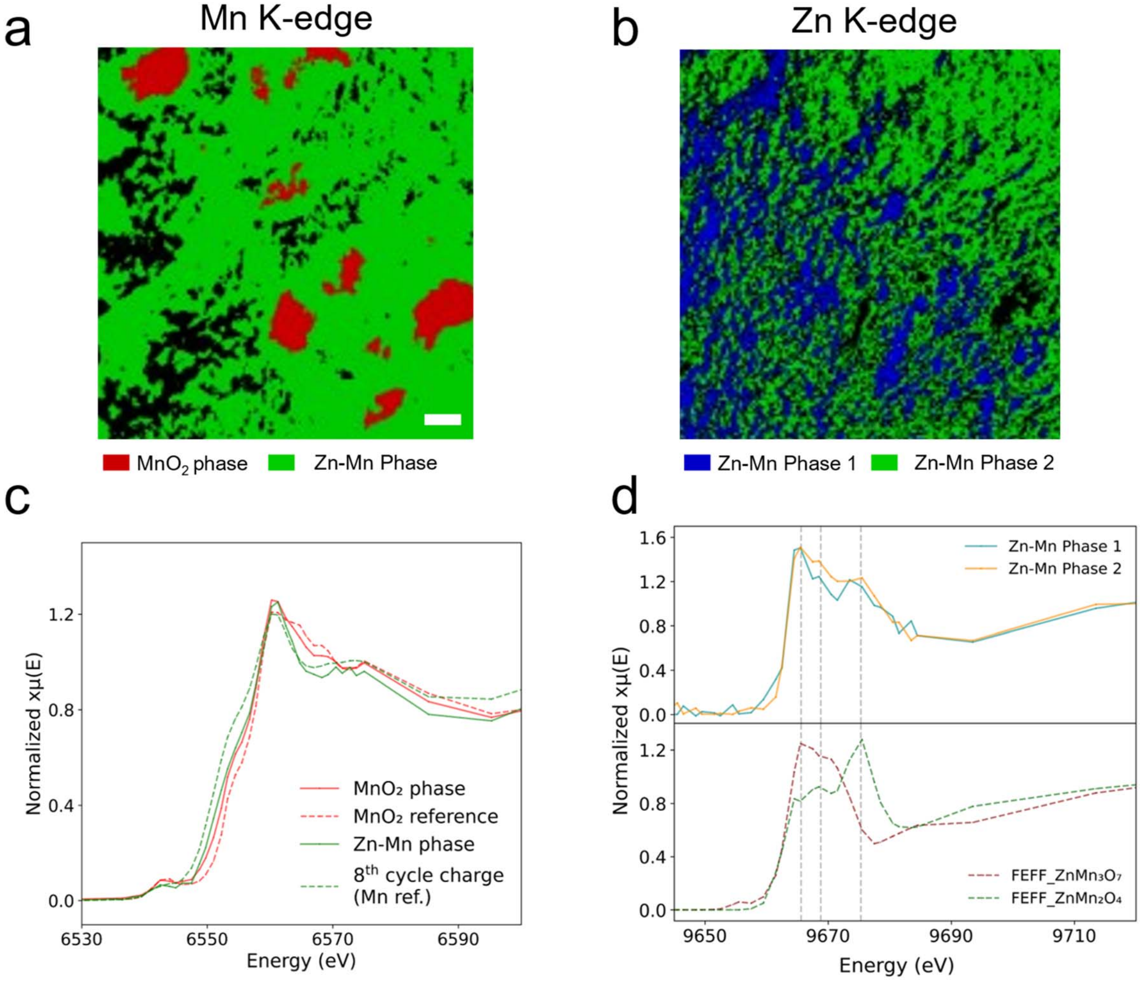

Fig. 5 Interpretation of the Mn and Zn chemical phases of ~160 hours cycled β-MnO_2 battery cathode. Surface view of the (a) two Mn phases and (b) two Zn-containing phases, obtained by K-means clustering of the XANES spectra in the 2D area of a β-MnO_2 ~160 hours cycled battery cathode. The scale bar in (a) and (c) corresponds to 2 μm. (c) The average spectra of the two areas obtained by K-means spectra corresponding to the MnO_2 (represented in red) and Zn–Mn complex phase (represented in green). (d) The average spectra of the three volumes obtained by K-means spectra corresponding to the Zn–Mn phase 1 (cyan), Zn–Mn phase 2 (orange).

surface. Each average spectrum shows varying ratios of three peaks, marked by the dotted vertical lines in Fig. 5d. Notably, the third peak in Zn–Mn phase 2 aligns with the $ZnMn_2O_4$ peak and is shifted to the right of the Zn–Mn phase 1 peak, suggesting a presence of structural variation in the two structures.

For the 3D XANES across the Mn K-edge, two XANES spectra were extracted based on the interpretation of the elbow plot in Fig. S12a and c, which correspond to two chemical species similar to the mid-cycled XANES analysis is the undissolved MnO_2 and the Zn–Mn complex plot. Fig. 6a represents the 3D and 2D cross-section visualization of the two Mn-containing phases obtained by K-means clustering of all the XANES spectra in the 3D volume after ~400 hours cycled Zn/β-MnO_2 battery cathode. The 3D volume considered for studying the Mn and Zn chemical phases were isolated based on the significant morphological features. Most volumes of the electrode did not have MnO_2 particles because of the dissolution process, except for a few volumes where the particles were still present. The reason for the undissolved MnO_2 particle was further investigated. The undissolved MnO_2 seems to be present inside a shell with a gap between the particle and the Zn–Mn complex (see Fig. 6a).The average spectra of the two volumes obtained by K-means spectrum corresponding to the MnO_2 (represented in red) and Zn–Mn complex (represented in green) (see Fig. 6b). Comparable to the 8th cycle charge sample the standard spectra corresponds to the Mn K-edge spectrum of pristine β-MnO_2 (represented in dotted red line) and 8th cycle charge electrode (represented in dotted green line) obtained from previous work.[21]

As the Zn–Mn complex is hypothesized to be a combination of two or more Zn-containing phases, the 3D XANES map across the Zn K-edge was used to further classify the different Zn phases within the Zn–Mn complex. The Zn K-edge spectra for the volume were classified into three phases based on the interpretation of the elbow plot (see Fig. S12b and d) and its scientific significance. Fig. 6c represents the 3D and 2D cross-section visualization of the three Zn-containing phases obtained by K-means clustering of the XANES spectra of the 3D

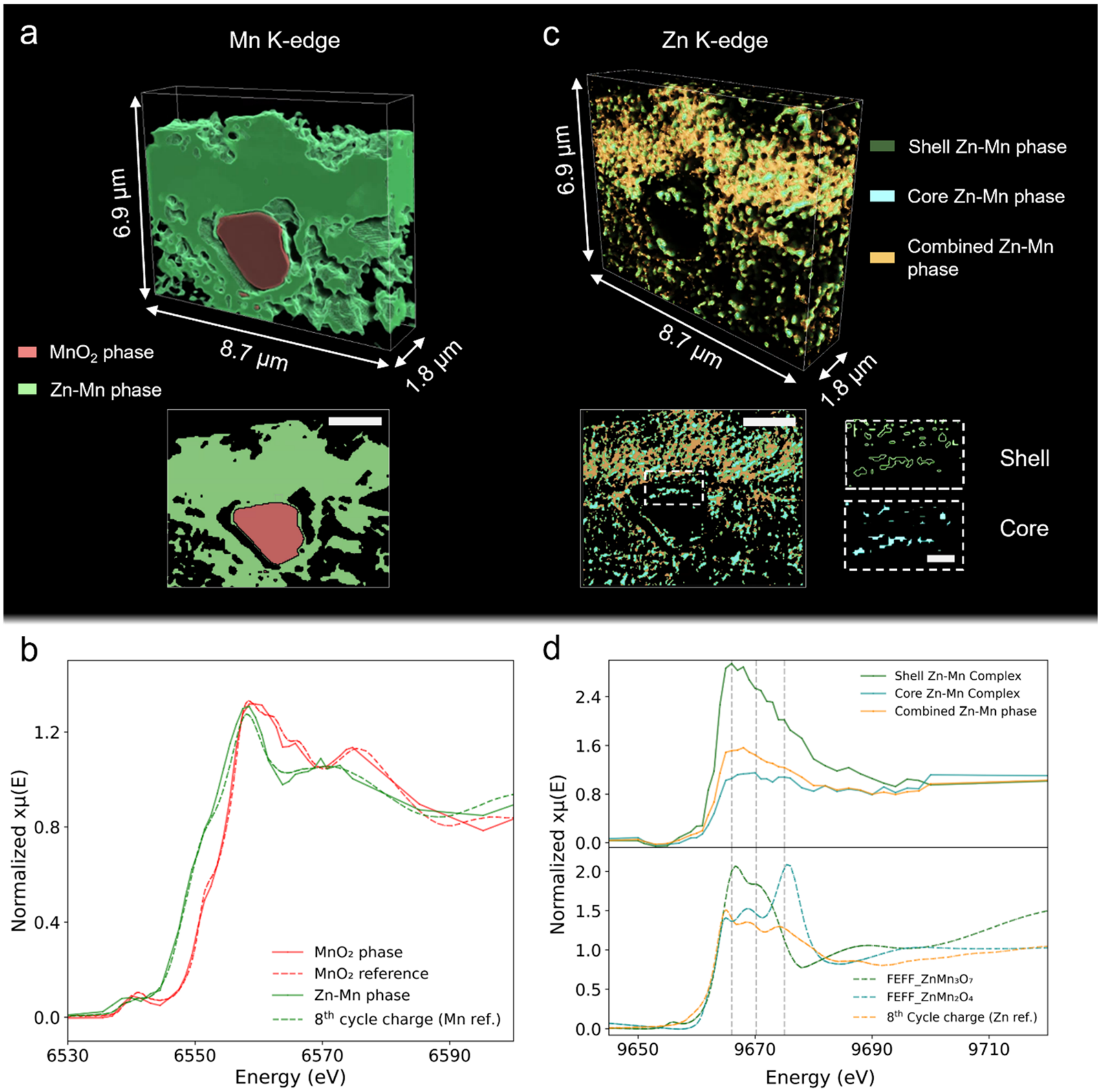

Fig. 6 Elucidation of the 3D Mn and Zn chemical phases of ~400 hours cycled β-MnO_2 battery cathode. 3D and 2D cross-section visualization of the (a) two Mn phases and (c) three Zn-containing phases obtained by K-means clustering of the XANES spectra in the 3D volume of a β-MnO_2 battery cathode. The 2D cross-section scale bar in (a) and (c) corresponds to 2 µm and 500 nm in the inset plot in (c). (b) The average spectra of the two volumes obtained by K-means spectra corresponding to the MnO_2 (represented in red) and Zn–Mn complex phase (represented in green). (d) The average spectra of the three volumes obtained by K-means spectra corresponding to the core (green), shell (cyan) and a combination of both shell and core Zn–Mn complex phases (yellow).

volume. Fig. 6d represents the average spectra of the three volumes obtained by K-means spectra corresponding to the shell, core and a combination of both Zn–Mn complex phases, respectively. The shell phase can be attributed to the Zn–Mn complex, namely the chalcophanite phase ($ZnMn_3O_7 \cdot 3H_2O$) and while the core Zn–Mn complex was attributed to the hetaerolite ($ZnMn_2O_4$) phase.[21,35,36] A comparison with the FEFF[21] calculated spectra of $ZnMn_2O_4$ and $ZnMn_3O_7$ with the average K means spectra is also shown in Fig. 6d. The dotted lines in Fig. 6d are used to identify the three peaks in the $ZnMn_2O_4$ spectrum calculated by FEFF in an increasing order, which is similar to the average spectra of the core Zn–Mn complex. In the case of FEFF calculated $ZnMn_3O_7$ spectrum, two peaks are identified, similar to the average spectra for the shell Zn–Mn complex. The third phase, termed the 'combined phase', is derived from the spectral summation of the core and shell Zn–Mn phases. For this phase, colocalization of the two Zn–Mn phases may be expected. Additionally, the average spectra could be compared to the bulk spectra from the 8th cycle charge MnO_2 electrode which contains both phases.[21]

As observed in the 3D and 2D views of Fig. 6c, the core phase (cyan) seems to be forming a clustered growth throughout the electrode. The surface of this phase is covered by the shell phase (green), resembling a shell-like structure as shown in the inset plot in Fig. 6c. A colocalized phase containing the shell and core phase (yellow) seems to be forming on the surface of the electrode. This is suggestive of a diffusive barrier which may be preventing the Mn and Zn ions diffusion into the electrolyte

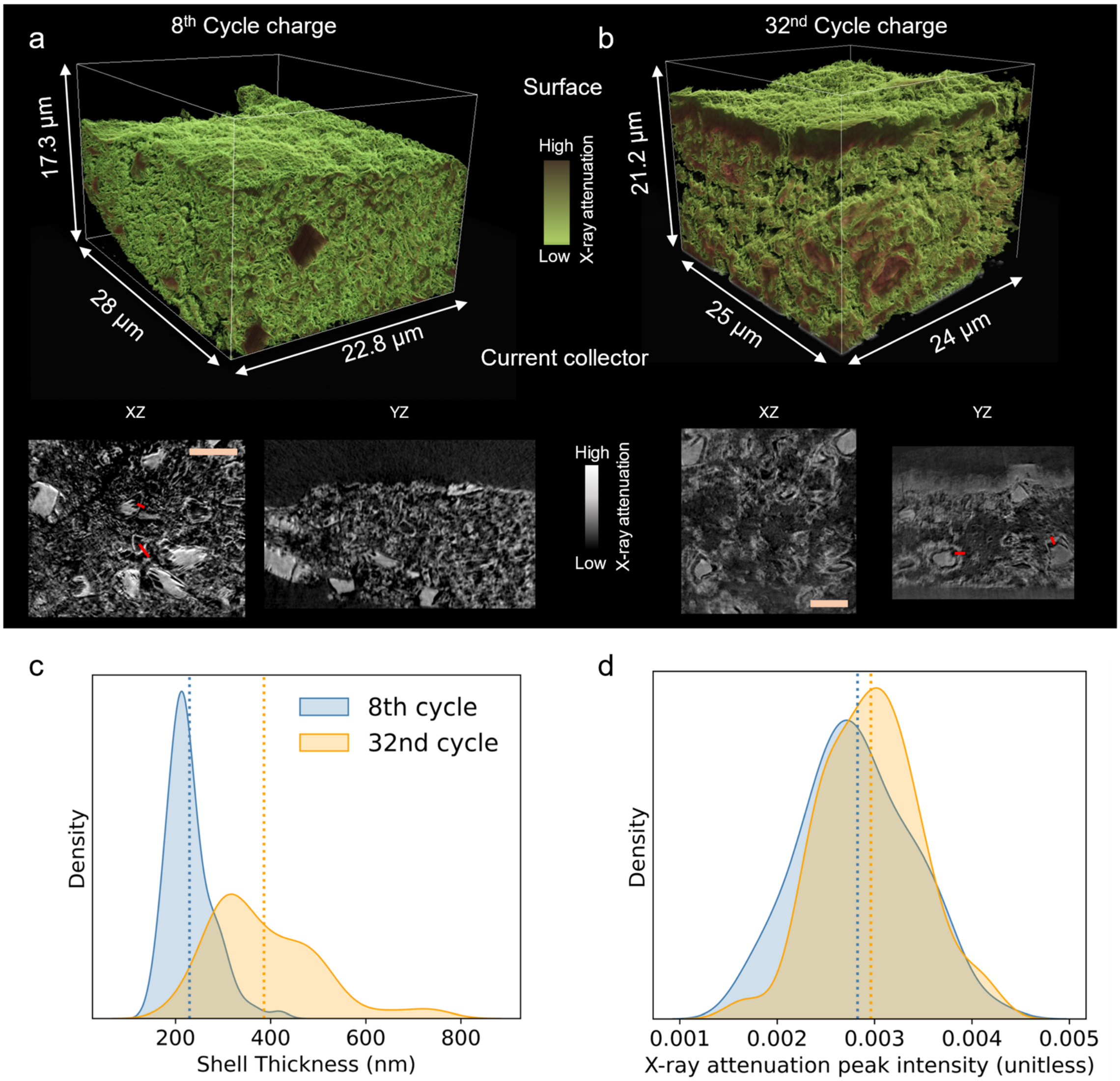

Fig. 7 Morphology and shell thickness of MnO_2 electrodes after ∼160 hours (8th cycle, mid-stage) and ∼400 hours (32nd cycle, later-stage) of cycling. (a and b) 3D X-ray nanotomography visualization charged MnO_2 electrodes after the 8th cycle (∼160 hours) (a) and 32nd cycle (∼400 hours) (b), along with two orthogonal cross-sectional views (*XZ*, *YZ*) highlighting interfacial morphology and internal porosity. Red arrows indicate regions with pronounced shell formation and contrast differences. Scale bar in these cross-sections indicate 5 µm. (c) Kernel density estimates of shell thickness and (d) X-ray attenuation intensity from Zn-rich shell regions, extracted from the 3D datasets.

which may attribute towards the capacity fade (see Fig. S11b). Additionally, an increase in pH in the Zn/MnO_2 battery with increase in cycles may lead to the formation of a terminal $ZnMn_2O_4$ phase, which could accumulate and inhibit further reactions.[21]

2.4 Morphology and shell thickness of MnO_2 electrodes after ∼160 hours (8th cycle, mid-stage) and ∼400 hours (32nd cycle, later-stage) of cycling

To further understand the morphological features of the chemically heterogeneous shell-like features observed after ∼160 hours (8th cycle) and ∼400 hours (32nd cycle) of cycling, we visualized the electrodes by 3D X-ray nanotomography. The electrode volumes (Fig. 7a and b) reveal distinct changes in the electrode architecture, with the ∼400 hours cycling electrode exhibiting a thicker, more irregular shell at the electrode–electrolyte interface compared to the electrode cycled until ∼160 hours (8th cycle). The orthogonal cross-sections (*XZ* and *YZ*) further emphasize this transformation, where dense shell-like features and higher attenuation regions become more prevalent. These changes indicate the progressive buildup of Zn–Mn rich species, forming a heterogeneous shell structure over time. Notably, red lines mark localized zones of shell growth, underscoring the spatial non-uniformity of interfacial evolution especially in the ∼160 hours cycled electrode.

Quantitative analysis of shell thickness and X-ray attenuation of the electrodes across the two cycles supports these observations. As shown in the kernel density estimates (Fig. 7c), the shell thickness distribution broadens and shifts toward higher values after ∼400 hours of cycling, with the mean thickness increasing from ∼230 nm to ∼390 nm. This

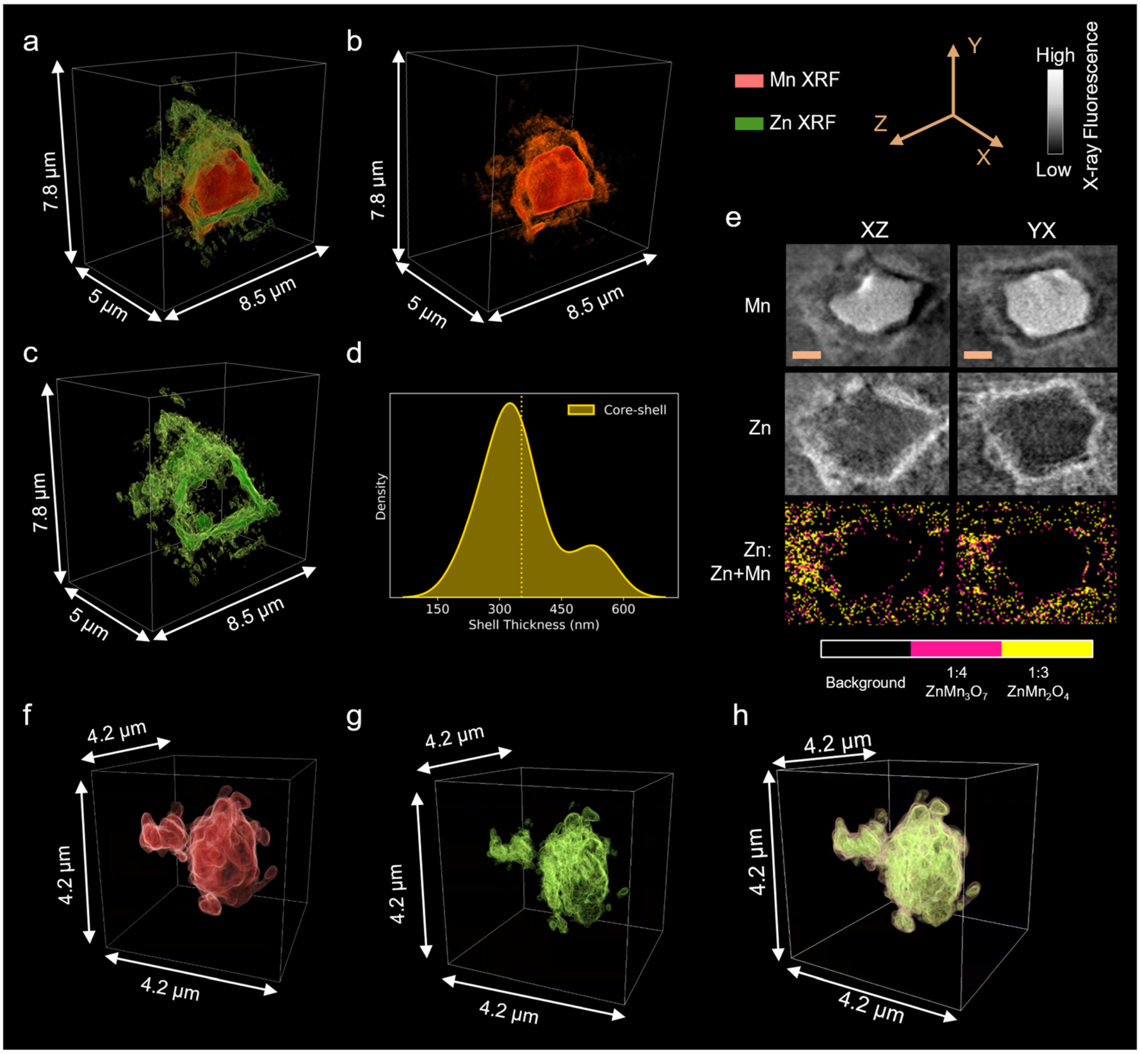

Fig. 8 X-ray fluorescence (XRF) nano-imaging reveals spatially resolved Zn–Mn distribution and shell-type structures in a long-cycled Zn/β-MnO$_2$ battery cathode. (a–c) 3D reconstructed XRF volumes showing overlaid Mn–Zn signals, Mn (red), Zn (green) of a shell around an undissolved MnO$_2$ particle. (d) Distribution of shell thickness, with a dominant thickness around 350 nm. (e) *XZ* and *YX* cross/sections to show the co-localization and Zn atomic ratio map in Zn and Mn highlighting phase heterogeneity in the shell, distinguishing ZnMn$_3$O$_7$ and ZnMn$_2$O$_4$-rich regions. (f–h) 3D XRF reconstructions of Zn–Mn aggregates, interpreted as ZnMn$_2$O$_4$ clusters. Scale bar in (e) corresponds to 1 µm.

morphological thickening likely reflects repeated dissolution and redeposition processes involving Zn–Mn complexes. Simultaneously, the X-ray attenuation intensity distribution shows a modest but noticeable increase, suggesting a compositional change possibly due to the accumulation of heavier Zn-containing species (Fig. 7d). Together, these findings highlight the heterogeneous evolution of MnO$_2$ electrode interface, which may contribute to capacity fade during extended cycling. Additional information of the kernel density estimates of shell thickness and intensity is described in the Experimental section 5.2.5.

2.5 X-ray nano-imaging reveals morphology of longer cycled electrode

The undissolved MnO$_2$ particles and surrounding regions in the electrode for the ~400 hours cycled Zn/β-MnO$_2$ battery cathode were further characterized by XRF nano-imaging using a synchrotron hard X-ray nanoprobe (see Fig. 8). The 3D reconstructions of Mn and Zn XRF signals (Fig. 8a–c) reveal a distinct shell-like Zn–Mn structure enveloping large, undissolved MnO$_2$ particles. This shell is attributed to colocalized Zn and Mn complex forming around the MnO$_2$ during the charge process, likely nucleating on a pre-existing ZHS phase. The emergence of this shell leads to spatial separation of the reactive interface, potentially limiting further electrochemical utilization of the MnO$_2$ due to poor contact with the electrolyte. The distribution of shell thickness (Fig. 8d) shows a dominant population ~300 nm and a mean thickness of ~350 nm, highlighting the extent of phase growth at the particle scale. This is consistent with the average shell thickness observed across particles throughout the electrode, as shown in Fig. 7c.

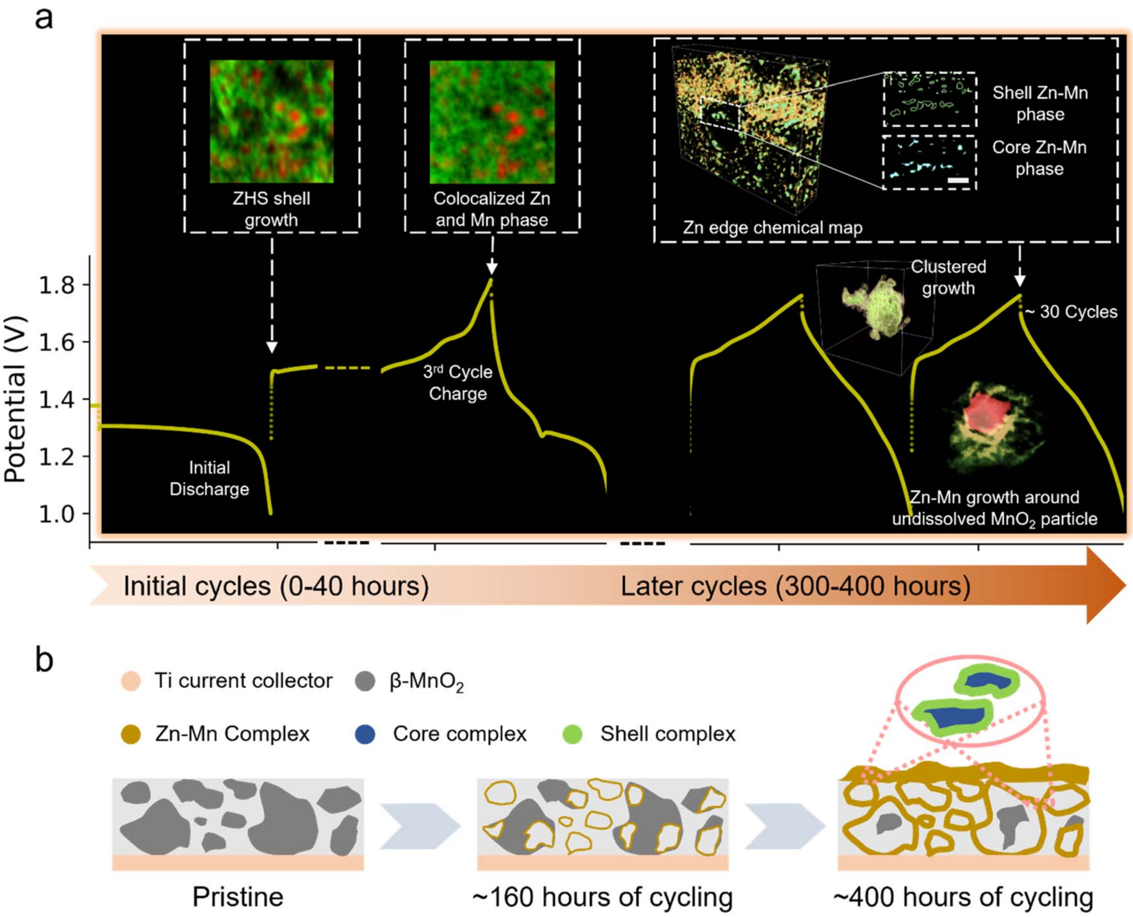

Fig. 9 A schematic illustrating the significant mesoscale morphological evolution of the Zn/β-MnO_2 battery throughout its operation. (a) Summary of key mechanistic insights related to chemical transformations during extended cycling. (b) Mesoscale schematic depicting how the initially uniform electrode evolves into a porous structure with Zn–Mn shell-like domains around undissolved MnO_2 particles after ~400 hours of cycling (later-cycle stage), impacting ion transport and contributing to capacity fade.

Cross-sectional views and compositional map of Zn atomic ratio in Zn and Mn (denoted as Zn : Zn + Mn atomic ratio) (Fig. 8e) indicate the formation of mixed-valent Zn–Mn phases, with regions consistent with $ZnMn_3O_7$ and $ZnMn_2O_4$ structures. These results, obtained *via* a different modality, further support the complex phase behavior described by the 3D chemical speciation analysis in Fig. 6. The dense aggregation of the $ZnMn_2O_4$ nanoclusters may reduce accessible surface area and hinder reversibility, further contributing to performance degradation upon prolonged cycling.

In addition to these core–shell structures, a second type of Zn–Mn morphology was observed within the electrode bulk. As shown in Fig. 8f–h, Zn and Mn are colocalized in nanoscale spherical clusters, which appear agglomerated and poorly dispersed.[21,36]

3. Conclusion

This study captures the dynamic processes occurring within the battery, revealing continuous chemical and morphological evolution. The spatial distribution of Zn and Mn containing complexes in aqueous Zn/MnO_2 is discussed using complementary element and phase sensitive *operando* and *ex situ* 2D and 3D X-ray synchrotron microscopy. The spatial distribution of the reaction products is characterized and discussed in this work, revealing the prevalence of ZHS and a subsequent formation of Zn–Mn phases. The formation of the ZHS phase during discharge may be important, as they act as the substrate for the deposition of the charged species. The ZHS phase was observed to form in close vicinity of the dissolution of the MnO_2 particles, suggesting that the initial electrode morphology may influence the local reaction environment and subsequent product evolution. With subsequent cycles the growth and build-up of Zn–Mn complex is visible in the vicinity of the particles. The interfacial shape distribution based on the curvature analysis of the surface of large MnO_2 particles during the quasi-*in situ* electrochemical process quantified variations in surface roughness throughout the discharge and charge states. This enhanced understanding indicates the crystalline nature of ZHS and suggests that the charge product may be amorphous due to its smoother structure.

To differentiate the spatial growth of the different chemical species forming in the electrode and to understand the Zn/MnO_2 battery failure mechanism, mid-cycled electrode ~160 hours and long cycled electrode for ~400 hours cycled MnO_2

electrode was studied using XANES imaging. The mid-cycled electrodes showed heterogeneity indicating a complex phase containing two different proportions of the $ZnMn_3O_7$ and $ZnMn_2O_4$ phases. For the ∼400 hours cycled electrode, K-means clustering of the Mn K-edge spectra indicates the presence of undissolved MnO_2 particles and Zn–Mn complex phase. The clustering of the Zn K-edge spectra further classified the cycled sample into shell and core Zn–Mn complexes. The Zn K-edge chemical map indicates that a thick Zn–Mn phase forms on the surface of the electrode which may cause a diffusion barrier for the Zn and Mn ions leading to the capacity fade of the battery. In addition, the shell phase ($ZnMn_3O_7$) seems to be forming a shell over the clustered growth of the core phase ($ZnMn_2O_4$). This analysis was able to delineate the chemical species forming in the bulk in the vicinity of the undissolved particles and the interface of the aqueous Zn/MnO_2 batteries which dictate future reaction. X-ray fluorescence nano-imaging enabled the visualization of the Zn–Mn complexes forming a shell-like structure around unreacted MnO_2 particles, indicative of reaction heterogeneity. The Zn atomic ratio in Zn and Mn maps obtained by X-ray fluorescence imaging further supports the complex phase behavior revealed by the 3D chemical speciation analysis of the shell by XANES imaging. Fig. 9a provides a schematic illustration summarizing the significant morphological evolution of $Zn/\beta\text{-}MnO_2$ battery.

To complement these insights, Fig. 9b illustrates the corresponding mesoscale transformation of electrode architecture. The schematic shows how the initially uniform electrode surface evolves into a porous matrix with embedded Zn–Mn growth sites after ∼400 hours of cycling. These Zn–Mn domains, shell-like features form preferentially around undissolved MnO_2 particles and are expected to impact on ionic transport, local reaction environments, and ultimately the long-term reversibility of the battery. Together, Fig. 9a and b capture the coupled chemical–morphological evolution underpinning capacity fading in aqueous $Zn/\beta\text{-}MnO_2$ systems.

Overall, this work highlights the spatial and chemical heterogeneity of the dissolution–deposition reaction mechanism in Zn/MnO_2 batteries, indicating that the ZHS phase formed during the initial discharge cycle plays a key role in guiding subsequent reactions. Therefore, the initial morphology and distribution of MnO_2, as well as the initial discharge rate leading to ZHS formation, are critical in determining battery performance. Building on these mechanistic insights, potential strategies to improve cycling stability include engineering MnO_2 at the nanoscale and integrating it into 3D conductive architectures to maintain electrochemical contact and reduce surface reaction losses over extended cycling.

The progressive thickening of the Zn–Mn shell suggests an increasing degree of irreversibility that may not be fully mitigated by electrode morphology alone. Prior studies suggest that rising local pH during extended cycling can thermodynamically favor the formation of lower-valent Zn–Mn complexes.[21] In this context, electrolyte stabilization strategies such as the use of organic co-solvents[37,38] or water-in-salt electrolytes[39,40] have shown promise in stabilizing electrode interfaces and enhancing reversibility. Controlling the formation and dissolution of ZHS, as well as the growth of Zn–Mn shell and core phases, thus holds considerable potential for improving the electrochemical performance of mild-aqueous Zn/MnO_2 batteries.

4. Experimental section

4.1 Electrode preparation and electrochemical characterization

The preparation of $\beta\text{-}MnO_2$ electrode slurries involved vortex-mixing the active material,$\beta\text{-}MnO_2$ (≥99%, Sigma-Aldrich), with carbon black (Super C65, MTI Cooperation) and polyvinylidene fluoride (PVDF) binder (Alfa Aesar) in 1-methyl-2-pyrrolidone (NMP) solvent (Alfa Aesar). The mixing was performed using a planetary mixer (THINKY centrifugal mixer ARM-310, Thinky USA). The slurry composition was maintained at a weight ratio of 70 : 20 : 10 for the active material, carbon black and PVDF, respectively. Additionally, the solid content in the slurry relative to the NMP solvent was approximately 0.7. The resulting slurry was cast onto 11.4 μm titanium foils (Goodfellow) using a doctor blade, ensuring a wet film thickness of 100 μm by adjusting the gap accordingly. The coated electrodes underwent a drying process in a vacuum oven for 60 °C for 24 hours, leading to a final electrode thickness of approximately 20 μm. The average mass loading of the dried electrodes was around ∼1.5 mg cm^{-2}. The same preparation method was employed for fabricating batteries used in laboratory testing as well as those analyzed at synchrotron beamlines.

For evaluating the electrochemical performance of aqueous $Zn\text{–}MnO_2$ batteries, CR-2032-coin cells were assembled in ambient conditions. The assembly sequence consisted of, $\beta\text{-}MnO_2$ cathode, Celgard 3500 separator, zinc anode (100 μm in thickness), stainless steel spacer, and wave spring. The electrolyte solution contained 2 M $ZnSO_4$ + 0.1 M $MnSO_4$, with approximately 45 μl of electrolyte introduced per cell. The same electrolyte formulation was consistently used in both electrochemical testing and synchrotron-based characterizations, as described in the subsequent sections. Charge and discharge tests were conducted using a Biologic VSP300 potentiostat with a voltage range of 1–1.8 V. The C rates were determined based on the MnO_2 mass and an experimental capacity of 150 mAh per g MnO_2, derived from electrochemical testing.

4.2 Synchrotron characterization

4.2.1. *Operando* X-ray fluorescence microscopy to study the elemental distribution.

X-ray fluorescence microscopy (XRF) experiment was conducted at the Sub-micron Resolution X-ray Spectroscopy beamline (SRX, 5-ID) at NSLS-II. The incident X-ray energy was 15 keV, focused onto the sample by a set of Kirkpatrick–Baez mirrors with a spot size of ∼0.5 μm × 0.5 μm. The XRF experiment was conducted by raster scanning the sample against the incident X-ray beam, and the full XRF spectrum from the sample at each scanned point (pixel) was collected by a silicon drift detector. During the *operando* XRF experiment, the $Zn\text{–}MnO_2$ coin cell was discharged and charged at C rate of C/10 for the first cycle and C/5 for the second to fourth cycle. The *operando* setup included a coin-cell battery with a Kapton window and the XRF scans were collected on the MnO_2 cathode side of the battery with each 60 × 60 μm image taking ~20 min. The coin-cell was rotated 30° about the rotation axis towards the XRF detector as seen in Fig. S1. The elemental distribution as the function of the electrochemical cycling was obtained using XRF microscopy by fitting the fluorescence spectra of each pixel using the PyXRF software.[41] To correct for incident beam fluctuations, each XRF map was normalized to the corresponding incident X-ray intensity.

4.2.2. *Operando* X-ray μ-diffraction to track MnO_2 particle dissolution. *Operando* X-ray μ-diffraction measurement was conducted at the Sub-micron Resolution X-ray Spectroscopy beamline (SRX, 5-ID) at NSLS-II in conjunction with *operando* X-ray fluorescence microscopy measurement during the third to fourth cycle. A 2D Dexela X-ray detector with pixel size 150 × 150 μm was utilized to collect the diffraction patterns in transmission mode. The coin-cell was rotated back to 0° along the rotation axis and moved 500 μm under the center position (see Fig. S1b). The three measurements were done every 30 min over an area of 20 × 20 μm with a step size of 0.5 μm measured in raster mode. The diffraction rings in each 2D image were azimuthally integrated and reduced to an intensity *vs.* 2θ (diffraction angle) plot *via* a Python-based program DIOPTAS.[42] The wavelength was 0.8266 Å (corresponding to an X-ray energy of 15 keV), where the sample to detector distance was first calibrated by using a ZnO standard. To identify the corresponding phases, the peak profiles were compared with the standard references provided by a commercial database including JADE and PDF-4+ 2023 (JCPDS-ICDD). For Fig. S3, the particle location was obtained by taking the index at maximum MnO_2 (110) peak intensity across the three μ-XRD maps. The median of all XRD maps was then subtracted from the local XRD map to obtain 2D XRD maps in Fig. S3.

4.2.3. Quasi-*in situ* X-ray nano-tomography to study morphological evolution. The synchrotron nanoimaging study was conducted at the Full-field X-ray Imaging Beamline (FXI, 18-ID) of National Synchrotron Light Source II (NSLS-II) at the Brookhaven National Laboratory. The X-ray incident energy used was 9.53 keV which corresponds to above Mn K-edge (6.539 keV) and below Zn K-edge (9.659 keV), providing optimal imaging contrast for the Mn and Zn complex phases. The images from the Transmission X-ray Microscope (TXM) at FXI Beamline were captured using a lens-coupled CCD detector with 2560 × 2160 pixels has a field of view of 46.8 μm × 55.48 μm ($h \times v$). A camera binning of 2 × 2 was used, resulting in an effective pixel size of 43.34 nm.

The quasi-*in situ* cell setup comprises of a 1.5 mm Kapton capillary with the MnO_2 and the Zn anode inserted at the either ends of the capillary. The capillary is filled with 2 M $ZnSO_4$ + 0.1 M $MnSO_4$ electrolyte and sealed with epoxy. A few millimeters gap is present in between both cathode and anode. At these electrochemical states the cell was disconnected for a brief period (approximately 30 min) during which the cell was placed on the sample stage of the transmission X-ray microscope and a tomography measurement was performed at an energy of 9.1 keV. This setup is hence called the quasi-*in situ* setup. The rotation speed during the tomographic fly scan was carefully chosen to minimize beam exposure without the compromise to the number of projections. The X-ray passes through the capillary, perpendicular to the cell geometry (cathode–anode). The electrochemistry was paused prior to every X-ray tomography measurement. For each tomography scan the exposure time and rotation speed were tuned such that we could capture ~600 projections, with a total acquisition time of 45 seconds per scan. The tomography projections were low pass filtered before reconstruction with the Gridrec algorithm, using the Python-based package Tomopy.[43,44]

A circular mask was applied to the 3D tomographic reconstruction stack images to select the region of interest within the center of the reconstructed volume with sufficient signal-to-noise ratio A 3D median filter was then applied with a window size of 3 to denoise the images. Image segmentation for every tomography reconstruction was conducted by applying a threshold, identified by analyzing the binary image obtained from using a range of thresholds. The binary images were analyzed to ensure no noise/artefacts were present for the threshold being used for further processing. The segmented binary images across different datasets were cropped to the same size for all further statistical analysis. After cropping, the binary images were further denoised by the application of despeckle, image opening, morphology operations in sci-kit image python package.[41] For preparing the histogram plot for the total number of small particles in different electrochemical states, the particles in each segmented volume were labelled and counted using measure operation in sci-kit image python package.[45] To study the morphological evolution of the larger particles, the particles greater than 99.9% volume were isolated and then visualized.

The curvature analysis was conducted using the Avizo 9.3 software. Surfaces for the three electrochemical states were generated based on the constrained smoothing method. Both curvatures were exported from these surfaces to calculate the ISD plots. The minimum and maximum principal curvatures for the ISDs were computed using python script that takes surface and the curvatures file from Avizo as input.[46] Additionally, the mean and gaussian curvatures were visualized in Avizo 9.3 software.

4.2.4. XANES imaging analysis: probe of chemical heterogeneity. The ~160 hours and ~400 hours cycled sample was obtained by extracting the MnO_2 cathodes in the 8th and 32nd cycle charge state in 2 M $ZnSO_4$ with 0.1 M $MnSO_4$ electrolyte at a C-rate of 0.1C. The battery electrodes cathodes were extracted at a specific electrochemical state followed by washing with HPLC-grade water. Subsequently, it underwent vacuum drying for 12 hours at 60 °C. The electrodes were then cut into triangles and mounted onto stainless steel pins for measurement transmission X-ray microscopy measurements.

4.2.4.1 2D XANES imaging analysis. For the samples extracted after *operando* XRF measurement and the 8th cycle charge state, the 2D XANES data were measured across the Mn and Zn K-edge. The 2D image dataset was analyzed using the pyXAS software.[47] A camera binning of 4 × 4 was used, resulting in an effective pixel size of 86.68 nm. The dataset was aligned by using a reference image and feature above the metal K-edge using the built-in StackReg method.[48] A physics informed machine learning model was implemented to improve the signal to noise ratio of the XANES image. A pre-edge normalization using a 2nd degree polynomial was used to fit the pre-edge. Subsequently K-means clustering masks were generated. The average spectrum of the regions with the masks were plotted. These were then further simplified by observing similarities in the spectral features, while the masks with average spectra having a high noise were considered as background based on suitable cutoffs. The final mask was visualized using python and the average spectra was normalized using Athena.[49]

4.2.4.2 3D XANES imaging analysis. For 3D XANES data processing across the Mn and Zn for the 32nd cycle charge electrode, X-ray tomography scans were measured across the Mn and Zn K-edges at the Full-field X-ray Imaging Beamline (FXI, 18-ID) of National Synchrotron Light Source II (NSLS-II) at the Brookhaven National Laboratory. All tomographic data were reconstructed using the same method mentioned previously. After reconstruction, reconstructed volumes were aligned three dimensionally by the following method. The Fourier Transform of the reference image and the target image was calculated to get the cross-correlation function in the frequency domain, and the maximum absolute value in the cross-correlation function determines the optimal offset for the two images. This was implemented using the python code developed in PyXAS.[47] Once aligned, a 3D region of interest was identified and cropped. All reconstructed 3D volumes were combined along the energy axis for Mn and Zn edges respectively, into two 4D matrices. A mask was implemented to refine the dataset for subsequent analysis. This mask was employed on two criteria designed to enhance the accuracy of data processing. Firstly, the maximum absorption within the XANES spectrum was evaluated to exclude regions lacking significant signal intensity and thereby mitigating the influence of background noise on the analysis. This criterion ensures that only data points with a substantial absorption peak, indicative of a meaningful concentration of the element of interest, are included for further examination. Secondly, the edge jump difference was calculated by deducing the average post-edge absorption value from the pre-edge absorption average. By applying the mask, regions representative of the concentration of the target element can be selected to improve the accuracy of the subsequent analysis. An additional mask was applied to the Zn XANES data since it exhibited more subtle changes in the spectral features. A Savitzky–Golay filter with a window length of 5 and a polynomial order of 3 was applied to the spectrum for smoothing. The smoothed data was then normalized by setting the pre-edge to 0 and the post-edge to 1. The mask was updated post-normalization based on two conditions. The regions between −0.5 and 10 were considered as the sample, and all spectral points with zero intensity were appended to the mask. A K-means clustering algorithm was implemented using Scikit-learn package in python[33] on each of the 4D matrix with an initial guess of the number of clusters of three for Mn and four for Zn. The clustering technique classified the 3D volume into a background phase and distinct sub-volumes, each corresponding to different chemical species. The XANES data obtained from the sub-volumes were averaged followed by smoothening using a Savitzky–Golay filter with a window length of 5 and polynomial order of 3 prior to normalization to get the average spectrum for two different Mn. The XANES data obtained from the sub-volumes were averaged before normalization to get the three Zn phases. After isolating the sub-volumes with different chemical species, the 3D visualizations of the chemical distribution in post-cycled Zn–MnO_2 electrodes were rendered using Dragonfly software (version 2020.1, Comet Technologies Canada Inc.) for both Mn and Zn complex phases.

4.2.5. Shell thickness and intensity analysis of MnO_2 electrodes after ∼160 hours and ∼400 hours of cycling. Mesoscale tomography visualizations were generated by reconstructing tomograms from transmission X-ray microscopy collected at 9.8 keV, above Zn K-edge of both electrode states (after 8th cycle, ∼160 hours and after 32nd cycle, ∼400 hours cycling respectively) using the same method described in Section 5.2.3. The distribution of shell thickness was quantified by measuring the full width at half maximum (FWHM) of line profiles, randomly selected from approximately 100 measurements using ImageJ software.[50] The X-ray attenuation intensity was obtained by extracting the peak value along the line profile used to obtain the shell thickness. These measurements were used to generate kernel density estimate (KDE) plots using custom Python scripts, including the use of Seaborn package.[51]

4.2.6. Nano XRF image analysis. The MnO_2 electrodes used for nano-XRF measurement after ∼400 hours (after 32nd cycle) of cycling was the same sample analyzed in the 3D XANES imaging described above. The dried electrode was directly scraped from the current collector onto a sample mounting diving board. During data acquisition at the Hard X-ray Nanoprobe (HXN) beamline, a focused X-ray nanobeam was achieved using a Fresnel zone plate (FZP). The sample was measured in fly-scan mode at 10 keV. The zone plate utilized in this measurement had an outermost zone width of 30 nm and a diameter of 250 μm. The focus size was ∼40 nm, and the dwell time per scan point was 0.03 seconds.

Two locations within the same sample corresponding to the Zn–Mn shell around the undissolved MnO_2 particles were measured: the clustered Zn–Mn complex predominantly the $ZnMn_2O_4$ phase, at a scanning step size of 30 nm and 120 nm, with projections collected every 2° from 90° to −90° to demonstrate super-resolution imaging enhancement; the other at a scanning step size of 50 nm and 200 nm, with projections collected every 3° from 90° to −18° for fine-tuning. Fluorescence signals were collected using an energy-dispersive detector. XRF projections were aligned using pyStackReg[48] python package on the Zn XRF projections and then the same shifts were applied to the Mn XRF projections dataset. Subsequently, the tomography reconstruction was conducted using the Gridrec algorithm, implemented in a Python-based package Tomopy.[43,44] The reconstructed views were visualized using the Dragonfly software version 2020.1, Comet Technologies Canada Inc.

The shell thickness was estimated by calculating the full width at half maximum (FWHM) of line profiles, manually extracted from approximately 40 measurements of the image stack, following the same procedure described in Section 5.2.5. The Zn : Zn + Mn was obtained by normalizing the Mn and Zn XRF by the atomic X-ray cross-sections obtained from the pyXRF software.[41]

Conflicts of interest

There are no conflicts to declare.

Data availability

All the data relevant for the current submission entitled "Spatial and chemical heterogeneity in aqueous Zn/MnO_2 batteries: role of Zn and Mn containing complexes" are available upon request *via* email to the corresponding author Yu-chen Karen Chen-Wiegart.

The SI file includes figures and videos supporting the findings of this study. See DOI: **https://doi.org/10.1039/d5ta02014j**.

Acknowledgements

This research was supported by the Center for Mesoscale Transport Properties, an Energy Frontier Research Center supported by the U.S. Department of Energy, Office of Science, Basic Energy Sciences, under award #DE-SC0012673. This research used resources, Submicron Resolution X-ray Spectroscopy beamline (SRX, 5-ID), Full Field X-ray Imaging beamline (FXI, 18-ID) and Hard X-ray Nanoprobe beamline (3-ID) of the National Synchrotron Light Source II, a U.S. Department of Energy (DOE) Office of Science by Brookhaven National Laboratory under Contract No. DE-SC0012704. Part of the student effort from X. Zheng was supported by the Imaging and Microscopy Program at the National Synchrotron Light Source II of Brookhaven National Laboratory specifically for the super-resolution imaging enhancement. We thank the support of Data Science and System Integration staff, Steven LaMarra and beamline staff, John Trunk for setting up *operando* experiment. EST acknowledges the support of the William and Jane Knapp Chair of Energy and the Environment. We thank the HXN beamline team members for the instrumentation development.

References

1 Z. Yang, J. Zhang, M. C. W. Kintner-Meyer, X. Lu, D. Choi, J. P. Lemmon and J. Liu, *Chem. Rev.*, 2011, **111**, 3577–3613.

2 B. Dunn, H. Kamath and J.-M. Tarascon, *Science*, 2011, **334**, 928–935.

3 D. H. Doughty, P. C. Butler, A. A. Akhil, N. H. Clark and J. D. Boyes, *Electrochem. Soc. Interface*, 2010, **19**, 49.

4 D. Larcher and J. M. Tarascon, *Nat. Chem.*, 2015, **7**, 19–29.

5 X. Ji, *Energy Environ. Sci.*, 2019, **12**, 3203–3224.

6 X.-B. Cheng, R. Zhang, C.-Z. Zhao and Q. Zhang, *Chem. Rev.*, 2017, **117**, 10403–10473.

7 C. Liu, F. Li, L.-P. Ma and H.-M. Cheng, *Adv. Mater.*, 2010, **22**, E28–E62.

8 A. Konarov, N. Voronina, J. H. Jo, Z. Bakenov, Y.-K. Sun and S.-T. Myung, *ACS Energy Lett.*, 2018, **3**, 2620–2640.

9 M. Song, H. Tan, D. Chao and H. J. Fan, *Adv. Funct. Mater.*, 2018, **28**, 1802564.

10 G. Fang, J. Zhou, A. Pan and S. Liang, *ACS Energy Lett.*, 2018, **3**, 2480–2501.

11 N. Zhang, F. Cheng, Y. Liu, Q. Zhao, K. Lei, C. Chen, X. Liu and J. Chen, *J. Am. Chem. Soc.*, 2016, **138**, 12894–12901.

12 B. Tang, L. Shan, S. Liang and J. Zhou, *Energy Environ. Sci.*, 2019, **12**, 3288–3304.

13 Y. Zhu, G. Liang, X. Cui, X. Liu, H. Zhong, C. Zhi and Y. Yang, *Energy Environ. Sci.*, 2024, **17**, 369–385.

14 M. Chamoun, W. R. Brant, C.-W. Tai, G. Karlsson and D. Noréus, *Energy Storage Mater.*, 2018, **15**, 351–360.

15 B. Lee, H. R. Seo, H. R. Lee, C. S. Yoon, J. H. Kim, K. Y. Chung, B. W. Cho and S. H. Oh, *ChemSusChem*, 2016, **9**, 2948–2956.

16 Y. Huang, J. Mou, W. Liu, X. Wang, L. Dong, F. Kang and C. Xu, *Nano–Micro Lett.*, 2019, **11**, 1–13.

17 I. A. Rodríguez-Pérez, H. J. Chang, M. Fayette, B. M. Sivakumar, D. Choi, X. Li and D. Reed, *J. Mater. Chem. A*, 2021, **9**, 20766–20775.

18 N. Zhang, F. Cheng, J. Liu, L. Wang, X. Long, X. Liu, F. Li and J. Chen, *Nat. Commun.*, 2017, **8**, 1–9.

19 M. H. Alfaruqi, V. Mathew, J. Gim, S. Kim, J. Song, J. P. Baboo, S. H. Choi and J. Kim, *Chem. Mater.*, 2015, **27**, 3609–3620.

20 D. R. Wu, L. M. Housel, S. J. Kim, N. Sadique, C. D. Quilty, L. J. Wu, R. Tappero, S. L. Nicholas, S. Ehrlich, Y. M. Zhu, A. C. Marschilok, E. S. Takeuchi, D. C. Bock and K. J. Takeuchi, *Energy Environ. Sci.*, 2020, **13**, 4322–4333.

21 V. R. Kankanallu, X. Zheng, D. Leschev, N. Zmich, C. Clark, C.-H. Lin, H. Zhong, S. Ghose, A. M. Kiss, D. Nykypanchuk, E. Stavitski, E. S. Takeuchi, A. C. Marschilok, K. J. Takeuchi, J. Bai, M. Ge and Y.-c. K. Chen-Wiegart, *Energy Environ. Sci.*, 2023, **16**, 2464–2482.

22 H. Chen, C. Dai, F. Xiao, Q. Yang, S. Cai, M. Xu, H. J. Fan and S. J. Bao, *Adv. Mater.*, 2022, **34**, e2109092.

23 L. Godeffroy, I. Aguilar, J. Médard, D. Larcher, J.-M. Tarascon and F. Kanoufi, *Adv. Energy Mater.*, 2022, **12**, 2200722.

24 Z. R. Mansley, Y. Zhu, D. Wu, E. S. Takeuchi, A. C. Marschilok, L. Wang and K. J. Takeuchi, *Nano Lett.*, 2023, **23**, 8657–8663.

25 W. G. Lim, X. Li and D. Reed, *Small Methods*, 2023, 2300965.

26 D. Atkins, E. Capria, K. Edström, T. Famprikis, A. Grimaud, Q. Jacquet, M. Johnson, A. Matic, P. Norby, H. Reichert, J. P. Rueff, C. Villevieille, M. Wagemaker and S. Lyonnard, *Adv. Energy Mater.*, 2022, **12**, 2102694.

27 H. Moon, K. H. Ha, Y. Park, J. Lee, M. S. Kwon, J. Lim, M. H. Lee, D. H. Kim, J. H. Choi, J. H. Choi and K. T. Lee, *Adv. Sci.*, 2021, **8**, 2003714.

28 W. Liu, X. Zhang, Y. Huang, B. Jiang, Z. Chang, C. Xu and F. Kang, *J. Energy Chem.*, 2021, **56**, 365–373.

29 D. Wu, S. T. King, N. Sadique, L. Ma, S. N. Ehrlich, S. Ghose, J. Bai, H. Zhong, S. Yan, D. C. Bock, E. S. Takeuchi, A. C. Marschilok, L. M. Housel, L. Wang and K. J. Takeuchi, *J. Mater. Chem. A*, 2023, **11**, 16279–16292.

30 D. Kammer and P. W. Voorhees, *Acta Mater.*, 2006, **54**, 1549–1558.

31 J. Wang, Y.-c. Karen Chen-Wiegart, C. Eng, Q. Shen and J. Wang, *Nat. Commun.*, 2016, **7**, 12372.

32 K. P. Sinaga and M. S. Yang, *IEEE Access*, 2020, **8**, 80716–80727.

33 F. Pedregosa, G. Varoquaux, A. Gramfort, V. Michel, B. Thirion, O. Grisel, M. Blondel, P. Prettenhofer, R. Weiss and V. Dubourg, *J. Mach. Learn. Res.*, 2011, **12**, 2825–2830.

34 J. MacQueen, *Proceedings of the Fifth Berkeley Symposium on Mathematical Statistics and Probability, Volume 1: Statistics*, 1967, vol. 1, pp. 281–297.

35 S. J. Kim, D. Wu, L. M. Housel, L. Wu, K. J. Takeuchi, A. C. Marschilok, E. S. Takeuchi and Y. Zhu, *Chem. Mater.*, 2021, **33**, 7283–7289.

36 L. Li, T. K. A. Hoang, J. Zhi, M. Han, S. Li and P. Chen, *ACS Appl. Mater. Interfaces*, 2020, **12**, 12834–12846.

37 X. Liu, X. Dong, H. Adenusi, Y. Wu and S. Passerini, *Nat. Rev. Chem.*, 2025, **9**, 415–426.

38 W. Chen, Y. Wang, F. Wang, Z. Zhang, W. Li, G. Fang and F. Wang, *Adv. Mater.*, 2024, **36**, 2411802.

39 Z. Khan, D. Kumar and X. Crispin, *Adv. Mater.*, 2023, **35**, 2300369.

40 T. F. Burton, R. Jommongkol, Y. Zhu, S. Deebansok, K. Chitbankluai, J. Deng and O. Fontaine, *Curr. Opin. Electrochem.*, 2022, **35**, 101070.

41 L. Li, H. Yan, W. Xu, D. Yu, A. Heroux, W.-K. Lee, S. Campbell and Y. Chu, *PyXRF: Python-Based X-Ray Fluorescence Analysis Package*, SPIE, 2017.

42 C. Prescher and V. B. Prakapenka, *High Press. Res.*, 2015, **35**, 223–230.

43 D. A. Gürsoy, F. De Carlo, X. Xiao and C. Jacobsen, *J. Synchrotron Radiat.*, 2014, **21**, 1188–1193.

44 B. Dowd, G. Campbell, R. Marr, V. Nagarkar, S. Tipnis, L. Axe and D. Siddons, *Developments in Synchrotron X-Ray Computed Microtomography at the National Synchrotron Light Source*, SPIE, 1999.

45 S. van der Walt, J. L. Schönberger, J. Nunez-Iglesias, F. Boulogne, J. D. Warner, N. Yager, E. Gouillart, T. Yu and T. S.-I. Contributors, *PeerJ*, 2014, **2**, e453.

46 X. Zheng, X. Liu and Y.-c. K. Chen-Wiegart, Interfacial shape distribution calculation, Version 1.0.0, 2022, available at: **https://github.com/SBU-Chen-Wiegart/Interacial-shape-distribution-ISD**.

47 M. Ge and W.-K. Lee, *J. Synchrotron Radiat.*, 2020, **27**, 567–575.

48 P. Thévenaz, U. E. Ruttimann and M. Unser, *IEEE Trans. Image Process.*, 1998, **7**, 27–41.

49 B. Ravel and M. Newville, *J. Synchrotron Radiat.*, 2005, **12**, 537–541.

50 C. A. Schneider, W. S. Rasband and K. W. Eliceiri, *Nat. Methods*, 2012, **9**, 671–675.

51 M. Waskom, *J. Open Source Softw.*, 2021, **6**, 3021.